Spontaneous generation and active manipulation of real-space optical vortices

https://doi.org/10.1038/s41586-022-05229-4

Received: 4 February 2022

Accepted: 11 August 2022

Published online: 12 October 2022

Check for updates

Dongha Kim[1]✉, Arthur Baucour[2], Yun-Seok Choi[3], Jonghwa Shin[2] & Min-Kyo Seo[1]✉

Optical vortices are beams of light that carry orbital angular momentum[1], which represents an extra degree of freedom that can be generated and manipulated for photonic applications[2–8]. Unlike vortices in other physical entities, the generation of optical vortices requires structural singularities[9–12], but this affects their quasiparticle nature and hampers the possibility of altering their dynamics or making them interacting[13–17]. Here we report a platform that allows the spontaneous generation and active manipulation of an optical vortex–antivortex pair using an external field. An aluminium/silicon dioxide/nickel/silicon dioxide multilayer structure realizes a gradient-thickness optical cavity, where the magneto-optic effects of the nickel layer affect the transition between a trivial and a non-trivial topological phase. Rather than a structural singularity, the vortex–antivortex pairs present in the light reflected by our device are generated through mathematical singularities in the generalized parameter space of the top and bottom silicon dioxide layers, which can be mapped onto real space and exhibit polarization-dependent and topology-dependent dynamics driven by external magnetic fields. We expect that the field-induced engineering of optical vortices that we report will facilitate the study of topological photonic interactions and inspire further efforts to bestow quasiparticle-like properties to various topological photonic textures such as toroidal vortices, polarization and vortex knots, and optical skyrmions.

Vortices, which support non-trivial topological textures with singularities, have been demonstrated in various physical entities[18,19]. In condensed matter, vortices emerge from exotic physical phenomena, such as dipolar interaction in spintronics[20,21], polariton condensation in excitonics[22,23] and magnetic flux quantization in type-II superconductors[24,25]. Observation of their binding and unbinding phenomena, such as the Berezinskii–Kosterlitz–Thouless transition[26,27], introduced a new era in physics, which explored newly emerging phases of matter on account of the interactions between topological textures. The optical vortex (OV) is a topological texture in electromagnetic fields[1] with a zero-intensity singular point and a spiral phase front that has attracted immense attention as an optical analogy to the vortices of other physical entities. OVs have been demonstrated in a variety of forms, from free-propagating waves[28] to evanescent fields[29]. OVs support orbital angular momentum, and hence have been widely employed in fundamental studies and applications, such as spin–orbit interaction-mediated manipulation[2–4], forbidden electronic transition[5], classical and quantum information processing[6,7], and super-resolution microscopy[8].

However, conventional OVs have been implemented by employing fixed structural singularities, such as spiral phase plates[9], phased array antennas[10] and spatially engineered meta-surfaces[11,12], rather than critical phenomena. The use of fixed structural singularities prevents OVs from possessing quasiparticle-like behaviour, such as dynamic and interactive characteristics[13–17]. Recent studies have reported on the structural singularity-free generation of OVs, using the bound states in the continuum of photonic crystals[30,31] and the photorefractive response in a nonlinear bulk medium[32]; however, they were either implemented in the momentum space or were inappropriate for on-demand, external control. However, the topological vortices formed spontaneously in condensed-matter systems have taken advantage of spatially flexible and externally controllable behaviours. Thus, providing a platform for structural singularity-free generation and dynamic manipulation of real-space OVs will enable the investigation of topological interactions in photonics, including the topological Hall effect[33,34], chiral spin–orbit coupling[35,36] and topological phase transition[37,38], potentially leading to developments as rich as the condensed-matter vortices. In this study, we demonstrated the spontaneous generation of a real-space optical vortex and antivortex and their active control using an external magnetic field, at the heart of which is a gradient-thickness optical cavity (GTOC).

The GTOC consisted of a magneto-optic nickel (Ni) layer, between two silicon dioxide (SiO_2) layers, on top of an aluminium (Al) mirror (Fig. 1a). The thicknesses of the top and bottom SiO_2 layers, h_1 and h_2 respectively, gradually changed in almost orthogonal directions over the GTOC. The spatial area of the GTOC was mapped bijectively onto a part of the generalized parameter space of (h_1, h_2). The topological charge (w) is formed by encircling the reflection minimum in the parameter space (Fig. 1d). To induce the parameter-space topological texture and charge to the reflected light in the real space, we used the thickness gradients and covered the bijective area involving the targeted reflection minimum. The optical thickness of the Ni layer, which can be controlled by an external

[1]Department of Physics, KAIST, Daejeon, Republic of Korea. [2]Department of Materials Science and Engineering, KAIST, Daejeon, Republic of Korea. [3]Department of Chemistry, KAIST, Daejeon, Republic of Korea. ✉e-mail: dongha_kim@kaist.ac.kr; minkyo_seo@kaist.ac.kr

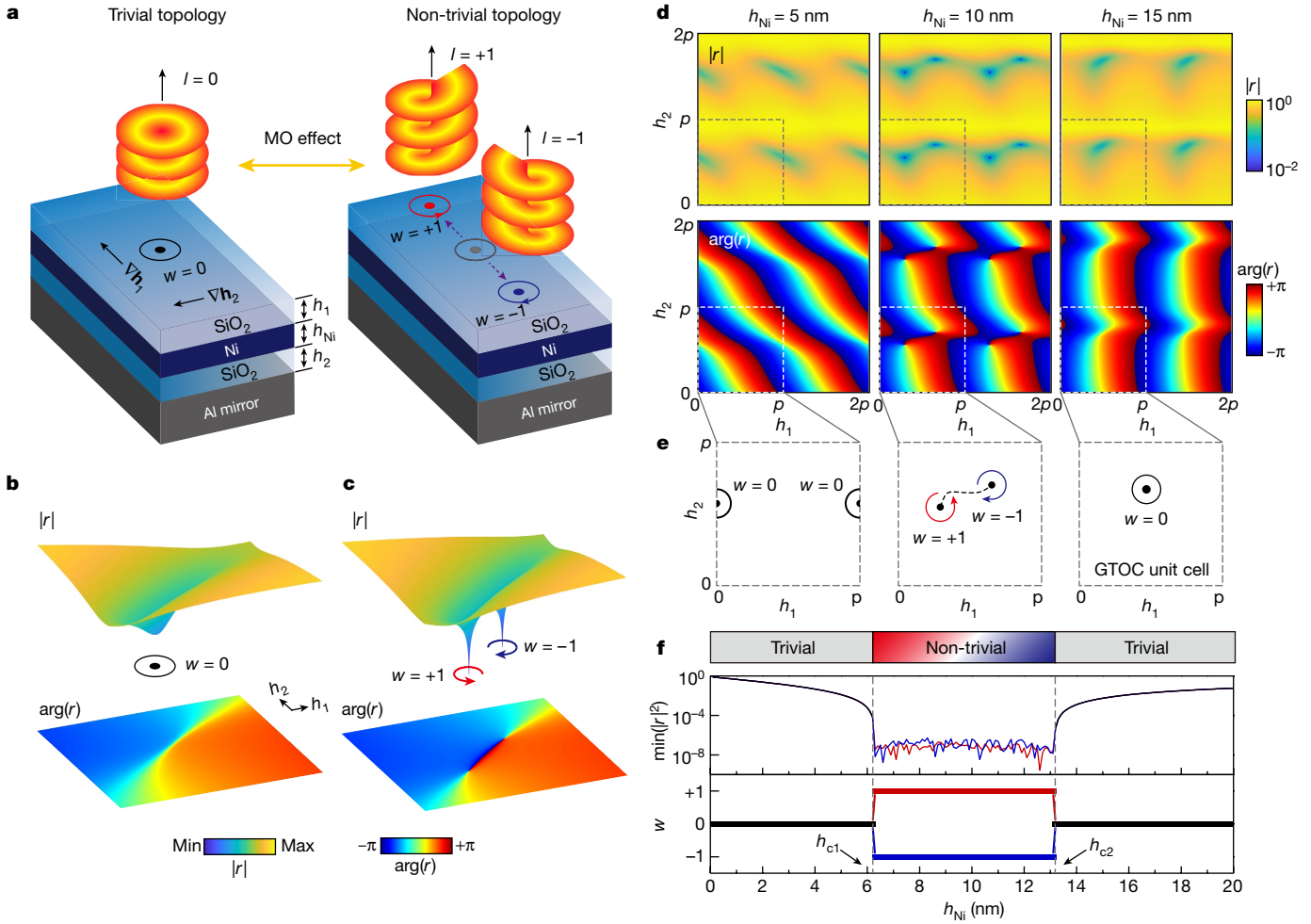

Fig. 1 | Magnetically controllable, spontaneous generation of an optical vortex–antivortex pair in a GTOC. a, Schematic illustration of trivial and non-trivial topological phases in the GTOC. The thicknesses of the top and bottom SiO_2 layers (h_1 and h_2) change in orthogonal directions. Changing the optical thickness of the Ni layer by the magneto-optic (MO) effects governs the transition between the trivial and non-trivial topological phases. l indicates the orbital angular momentum of the reflected light. **b**,**c**, Topological characteristics of the single weak minimum (**b**) and the singular vortex–antivortex pair (**c**). **d**, Calculated complex reflection coefficient distribution of the GTOCs with different Ni layer thicknesses (h_{Ni} = 5 nm, h_{Ni} = 10 nm and h_{Ni} = 15 nm) in the generalized parameter space (h_1, h_2). The topological texture repeats with a period of $p = \lambda/2n_{SiO2}$, and the dashed box indicates the GTOC unit cell. **e**, Description of the topology of the reflection minimum in the GTOCs of **d**. The black dashed line represents the branch cut between the vortex (red circular arrow) and antivortex (red circular arrow) singular points. **f**, Calculated reflectance ($\min(|r|^2)$), and topological charge (w) of the reflection minima depending on the Ni layer thickness (h_{Ni}).

magnetic field, characterized the topological texture of the reflected light from the GTOC. For most of the thickness range of the Ni layer, the GTOC exhibited a weak, non-zero minimum reflectance as a function of the thicknesses of the top and bottom SiO_2 layers (Fig. 1b). Enclosing the weak minimum, the texture of the complex reflection has zero topological charge ($w = 0$) and does not contain any notable features. We named this typical case the trivial topological phase. In contrast, for a specific range of Ni layer thicknesses, the GTOC exhibited a unique topological phase in reflection, that we called the non-trivial topological phase. The non-trivial topological phase has two singular points of zero reflection in the generalized parameter space, and their phase distributions support the optical vortex ($w = +1$) and antivortex ($w = -1$), respectively (Fig. 1c). This type of singularity originated from the mathematical topology around the zero-reflection solution in the generalized parameter space, and completely replaced the conventional structural singularity required to generate the optical vortex and antivortex. Moreover, the structural freedom of the GTOC in the topological singularity generation made it possible to actively create, annihilate and transport the optical vortex and antivortex by an external stimulus, that is, the applied magnetic field, as though they were quasiparticles.

Non-trivial topological phase of GTOC

The topological texture in the GTOC is periodically repeated depending on the thickness of the top and bottom SiO_2 layers (Fig. 1d). The periodicity (p) is given as $\lambda/2n_{SiO2}$, where λ and n_{SiO2} are the wavelength of light (632.8 nm) and the refractive index of SiO_2 (1.472), respectively. When the thickness of the Ni layer (h_{Ni}) was 5 nm, a weak reflection minimum was observed per unit cell ($p \times p$) in the generalized parameter space, without a phase singularity. The 5-nm-thick Ni layer was optically thin so that the reflection phase depended on the thickness of both the top and the bottom SiO_2 layers. The GTOC with h_{Ni} = 15 nm also exhibited a single weak reflection minimum in the unit cell; however, because of the optically thick Ni layer, the thickness of the top SiO_2 layer dominated the tendency of the reflection phase change. In contrast, the GTOC of h_{Ni} = 10 nm supported two singular points of extremely suppressed reflection in the unit cell, which possessed opposite topological charges ($w = \pm 1$), and created an optical vortex and antivortex pair. The Ni layer with an appropriate thickness allowed complete destructive interference between the optical fields in the top and bottom SiO_2 layers, which is the necessary condition for the singularity of zero reflection. Figure 1e

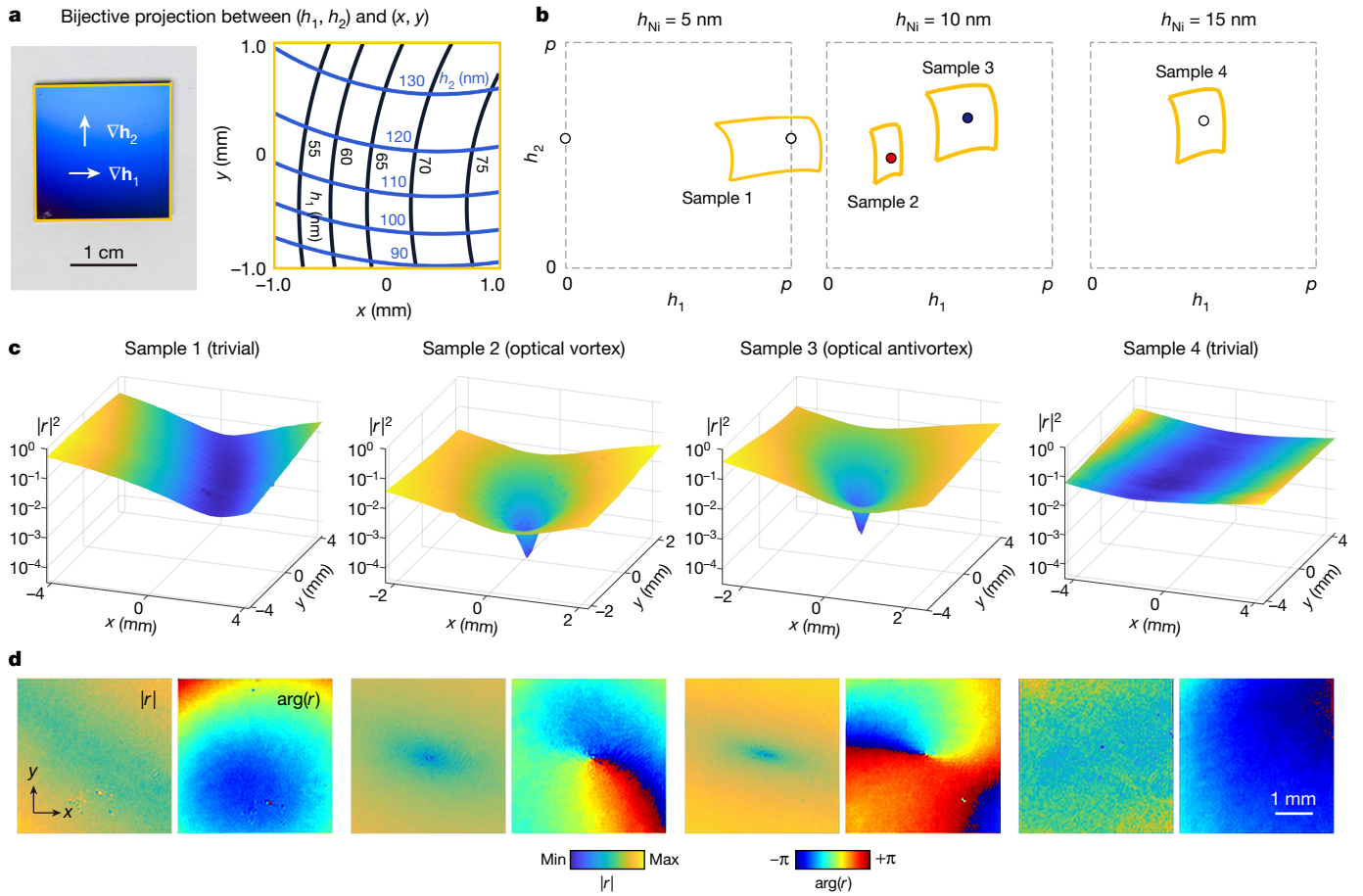

Fig. 2 | Measured trivial and non-trivial topological phases in the GTOC. **a**, Picture of a fabricated GTOC (sample 2), and the thickness distribution of the top and bottom SiO_2 layers measured using site-dependent ellipsometry. The black and blue lines indicate the equal-thickness curves of the top and bottom SiO_2 layers. **b**, Bijection of the areas of the employed GTOCs onto the generalized parameter space (h_1, h_2). Depending on the thickness of the Ni layer, each sample contains a weak or singular reflection minimum within its area (the solid yellow curved polygon) in the generalized parameter space. We investigated four different GTOCs (samples 1, 2, 3 and 4). The white circle indicates the weak reflection minimum of the trivial topological texture, and the red and blue circles indicate the singular reflection minima of the optical vortex and antivortex, respectively. **c**, Measured reflectance distribution of the four GTOCs under normal incidence. The wavelength of light is 633 nm. **d**, Measured amplitude (|r|), and phase (arg(r)) distribution of the complex reflection coefficient for the four GTOCs. Here, the right-handed (+σ) circularly polarized incidence was employed. The left-handed (−σ) circularly polarized incidence gives the same results (Extended Data Fig. 2).

shows the position and topological charge of the weak and singular minima of reflection in the generalized parameter space.

The solution of the singular zero reflection (r = 0) of the GTOC exists within a certain range of the Ni layer thicknesses. The multiple beam interference theory formulates the reflection coefficient by combining two participating terms: (1) optical paths including the propagations only above the Ni layer and (2) the other paths including the transmission through the Ni layer (Supplementary Section 1). The interference of the two terms enables us to analyse and understand the creation of the non-trivial topological phase. The singular minimum of reflection exists only when the two terms have the same amplitude and are out of phase. Each requirement appears as a closed loop (same amplitude condition) and finite curved lines (out-of-phase condition) in the generalized parameter space, resulting in a paired solution for the zero reflection at their intersections (Extended Data Fig. 1). Intersection of the same amplitude and out-of-phase condition was established only between two critical thicknesses of the Ni layer, h_{c1} = 6.29 nm and h_{c2} = 13.15 nm (Supplementary Video 1).

The evolution of the reflectance minimum and topological charge depending on the Ni layer thickness confirmed the topological phase transition of the GTOC (Fig. 1f). Here, the topological charge was determined by integrating the reflection phase along a closed path, enclosing the reflectance minimum in the generalized parameter space. For $h_{Ni} < h_{c1}$ ($h_{Ni} > h_{c2}$), a single reflectance minimum was observed, accompanied by the zero topological charge, and its value gradually decreased from 7.77×10^{-1} to 6.56×10^{-5} (from 5.78×10^{-2} to 5.60×10^{-6}) as h_{Ni} approached the critical thickness. For $h_{c1} < h_{Ni} < h_{c2}$, two reflection minima with w = +1 and w = −1 were observed, and their values on the order of 10^{-7} were three orders of magnitude smaller than that of the trivial weak reflection minimum. The transition between the trivial and non-trivial topological phases exhibited a discontinuity in the first derivative of the reflectance and topological charge value at the critical thicknesses. The Ni layer does not show a hysteresis behaviour to the external magnetic field (Supplementary Section 2). Without applying an external magnetic field, the complex reflection coefficient distributions are independent of the polarization state of the normal incidence. The non-trivial topological phase can emerge with a broad range of the incident angle and wavelength of light (Supplementary Section 3).

Demonstration of real-space OV at non-trivial phase

We experimentally demonstrated the trivial and non-trivial topological phases in the GTOCs with different Ni layer thicknesses (Fig. 2). We fabricated the samples on a square piece of Si substrate, by sequential deposition of the Al mirror, SiO_2 first layer (h_2), Ni and SiO_2 second layer (h_1)

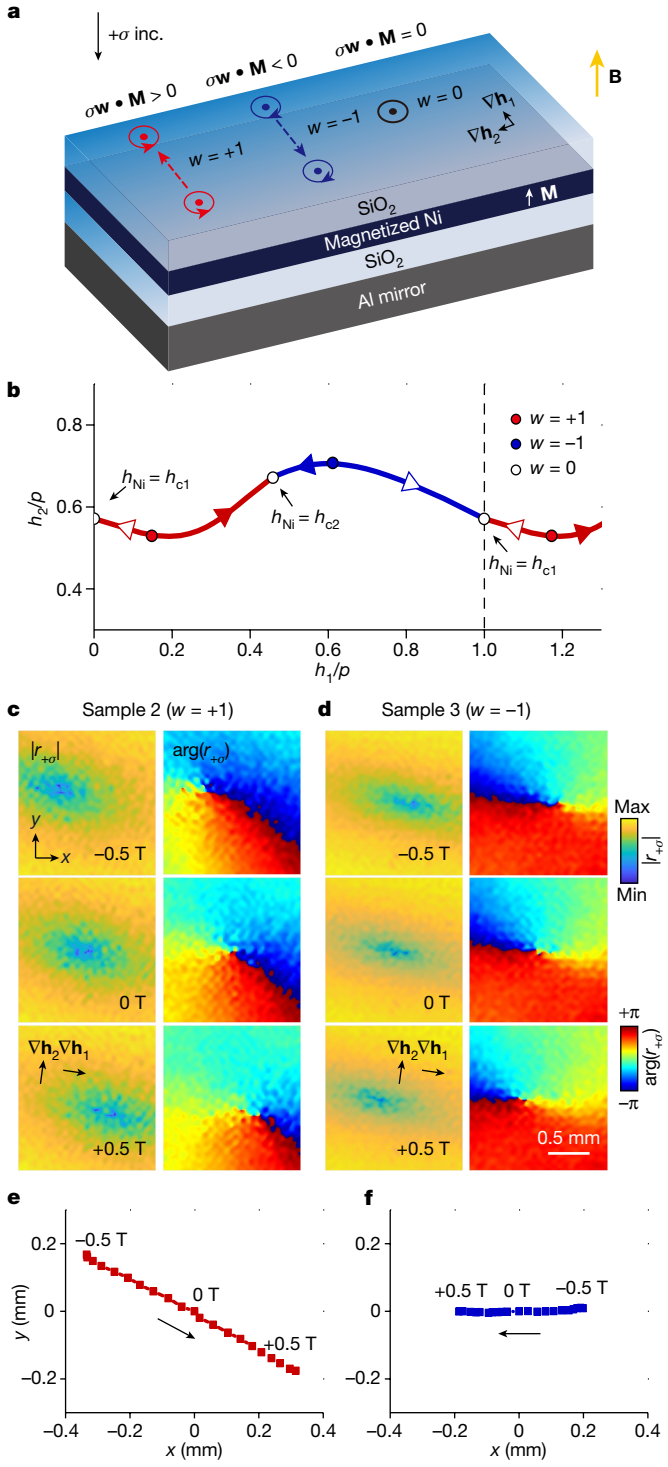

Fig. 3 | Magneto-optically driven dynamics of the optical vortex and antivortex controllable by the external magnetic field. a, Schematic illustration of the magneto-optically driven dynamics of real-space optical vortices in the GTOC. The parameter ($\sigma\mathbf{w}\cdot\mathbf{M}$) characterizes the dynamics of the optical vortex, antivortex and weak reflection minimum depending on the topological charge ($\mathbf{w} = w\hat{\mathbf{z}}$, $w = +1$, $w = -1$ and $w = 0$), the magnetization ($\mathbf{M}$) of the Ni layer induced by the external magnetic field, and the circular polarization state ($\sigma = +1$ and $\sigma = -1$) of light. **b**, Calculated trajectory of the singular reflection minima in the generalized parameter space. As the optical thickness of the Ni layer increases, the optical vortex (red circle, $w = +1$) and antivortex (blue circle, $w = -1$) emerge at the position of the weak reflection minimum (white circle, $w = 0$, $h_{Ni} = h_{c1}$), move along the different trajectories (solid triangles), and disappear at the position of the other weak reflection minimum ($h_{Ni} = h_{c2}$), and vice versa (open triangles). **c**,**d**, External magnetic field-dependent behaviour of the complex reflection coefficient ($r_{+\sigma}$) of the optical vortex and antivortex that sample 2 (**c**) and sample 3 (**c**) (the GTOCs of $h_{Ni} = 10$ nm in Fig. 2) support. **e**,**f**, Trajectories of the optical vortex (**e**) and antivortex (**f**) depending on the applied magnetic field.

(Fig. 2a). The SiO_2 layers exhibited a gradual change in thickness over the sample but the Ni layer was deposited uniformly over the sample area (Methods and Supplementary Section 4). The thickness gradients of the top and bottom SiO_2 layers (∇h_1 and ∇h_2) were engineered to be almost perpendicular, and their dimensionless magnitudes were on the order of nanometres per one millimetre. Under these conditions, the fabricated 2×2-cm^2-sized sample covered a partial area of the GTOC unit cell in the generalized parameter space (indicated region by the yellow line in Fig. 2b), which contained a weak or singular minimum of reflection. The bijective projection between the real and generalized parameter spaces was performed by considering the spatially varying magnitudes of the thickness gradients over the samples. In Fig. 2b, we examined four different samples (namely, samples 1, 2, 3 and 4) supporting the trivial weak minimum and the vortex–antivortex singularity predicted in Fig. 1d,e.

In Fig. 2c, we measured the reflectance of the GTOCs depending on their position using a confocal microscope. The GTOCs of $h_{Ni} = 5$ (sample 1) and $h_{Ni} = 15$ nm (sample 4) generated a weak reflection minimum with a reflectance of approximately 2.46×10^{-2} and 3.00×10^{-2}, respectively. Their reflectance distributions showed the behaviour of a normal differentiable function in two dimensions. In contrast, the GTOCs of $h_{Ni} = 10$ nm clearly produced a singular point in the reflectance distribution: $|r|^2 \approx 4.04 \times 10^{-5}$ (sample 2) and $|r|^2 \approx 2.30 \times 10^{-4}$ (sample 3). As previously mentioned, the existence of a non-differentiable reflectance extremum is necessary to support the phase singularity for an optical vortex or antivortex. The amplitude and phase distribution of the complex-valued reflection coefficient, $r(x, y)$, directly revealed the topological texture created by the GTOC (Fig. 2d). We measured the complex reflection coefficient distribution using off-axis holography (Methods and Supplementary Section 5). Samples 1 and 4 exhibited trivial topology without any phase singularity. However, samples 2 and 3 built anticlockwise and clockwise phase windings, corresponding to the optical vortex and antivortex, respectively, without any structural singularity. The orbital-angular-momentum purity of the vortex and antivortex in the experiment was evaluated to be about 86.6% and about 79.0%, respectively (Supplementary Section 6). From the measured reflectance distribution, we evaluated the power efficiency of the optical vortex and antivortex to be about 1.30% and about 6.99%, respectively, which can be improved up to 12.4% and 37.2%, respectively, by engineering the thickness gradients (Supplementary Section 7). The footprint of the optical vortex and antivortex can be reduced at the micrometre scale by increasing the thickness gradients of the GTOC (Supplementary Section 8).

Magneto-optically driven dynamics of real-space OVs

The GTOC activated topology-dependent magneto-optic dynamics of the optical vortex and antivortex, interacting with the external magnetic field (Fig. 3a). The off-diagonal term of the permittivity tensor sensitively responded to the induced magnetization ($\mathbf{M}$) in the Ni layer and caused a magnetic circular birefringence. We note that the use of high-Voigt-parameter materials such as cobalt (Co), iron (Fe) and permalloy (Py: Ni–Fe) will improve the magneto-optic performance of the GTOC platform. The magnetic birefringence enabled the engineering of the optical thickness of the Ni layer for the circularly polarized light. The optical thickness of the Ni layer governs the appearance of the non-trivial

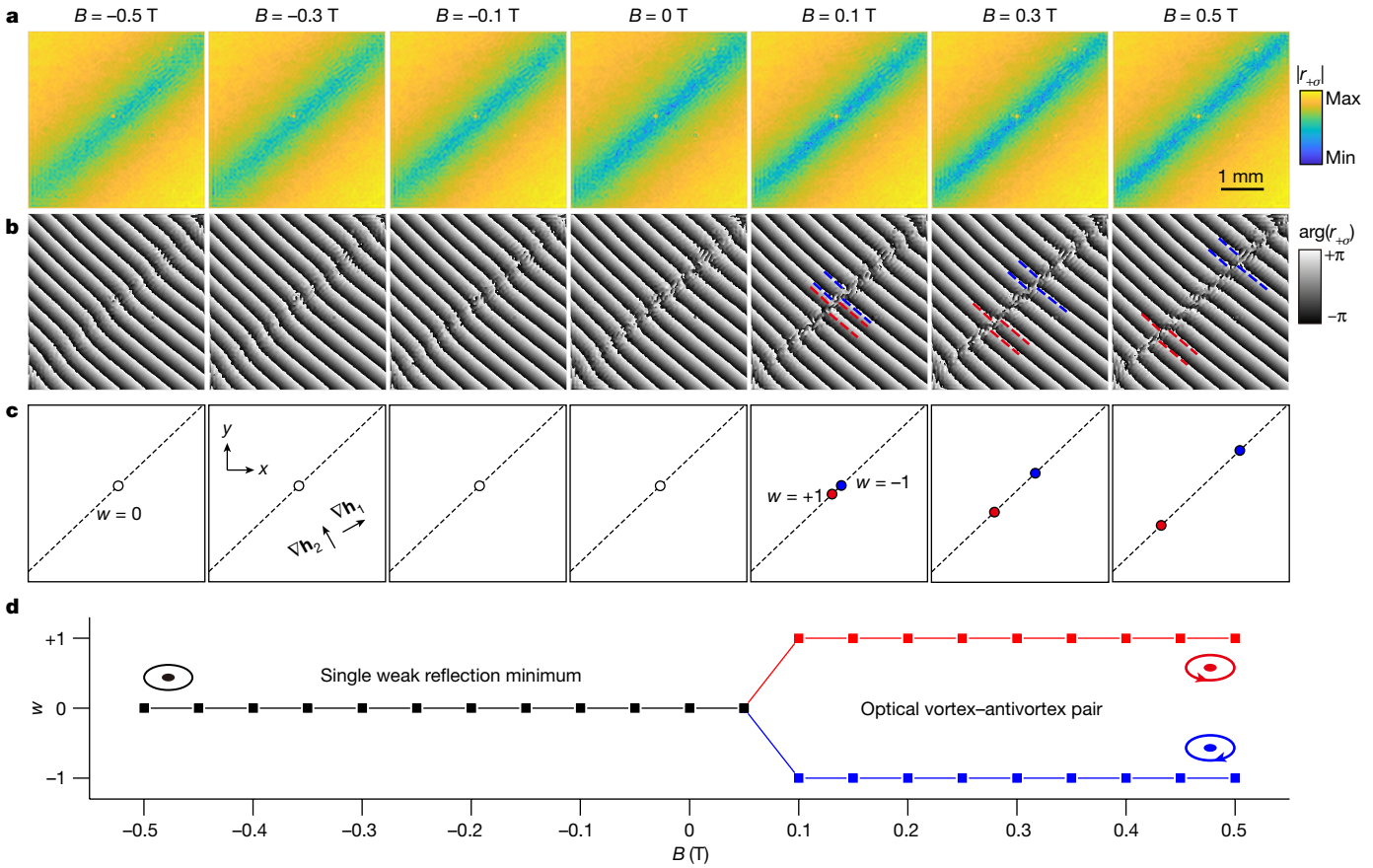

Fig. 4 | Magnetically induced generation and annihilation of optical vortex–antivortex pair. a,**b**, Measured reflection amplitude (**a**) and phase (**b**) distributions of the GTOC (sample 5, $h_{Ni} \approx 13$ nm) depending on the applied magnetic field. The phase distribution with an added continuously varying global phase clearly identifies the fork patterns of the optical vortex (dashed red guideline, $w = +1$) and antivortex (dashed blue guideline, $w = -1$). **c**, Trajectory of the topological texture depending on the magnetic field. The white circle indicates the position of the weak reflection minimum. The dashed guideline indicates the opposite-direction movements of the optical vortex (red circle) and antivortex (blue circle). **d**, Topological phase transition controlled by the external magnetic field. The sudden transition between the trivial (single weak reflection minimum) and non-trivial (optical vortex–antivortex pair) topological phases appears at the critical magnetic field of approximately 0.05 T.

topological phase in the GTOC and determines the position of the optical vortex and antivortex in the generalized parameter space and the corresponding real space. Depending on the topological charge ($\mathbf{w} = w\hat{z}$, where $\hat{z}$ is the unit vector along the out-of-plane direction, $w = +1$, $w = -1$ and $w = 0$), the out-of-plane magnetization ($\mathbf{M} = M\hat{z}$) of the Ni layer induced by the external magnetic field, and the circular polarization handedness ($\sigma = +1$ and $\sigma = -1$) of light, the magneto-optic effects governed the dynamic behaviour and movement of the topological texture in terms of $\sigma\mathbf{w} \cdot \mathbf{M}$. As the optical thickness of the Ni layer changed, the optical vortex and antivortex exhibited opposite movements. The vortex and antivortex mainly moved along the trajectory of the singular minimum solution depending on h_{Ni} (Fig. 3b). Owing to the circular birefringence, if the polarization of the incident light changes from the right-handedness to left-handedness, the movement and dynamics of the vortex–antivortex singularity emerge in the opposite direction (Extended Data Fig. 2). As the magnetization changed from the negative to the positive direction, the optical thickness of the Ni layer effectively increased (decreased), for the right-handed (left-handed) circularly polarized light. The optical vortex and antivortex arose at the critical thickness (h_{c1}) of the Ni layer, moved in opposite directions, and disappeared at the other critical thickness (h_{c2}), and vice versa.

Figure 3c,d shows the behaviours of the optical vortex (sample 2) and antivortex (sample 3), depending on the external magnetic field for the right-handed ($+\sigma$) circularly polarized light. When the external magnetic field changed from −0.5 T to +0.5 T, the optical vortex and antivortex showed movements in the real space as $(\Delta x, \Delta y) = (0.649$ mm, −0.344 mm) and (−0.385 mm, 0.010 mm), which can be projected onto the generalized parameter space as $(\Delta h_1, \Delta h_2) = (0.90$ nm, −0.58 nm) and (−1.03 nm, 0.18 nm), respectively (Fig. 3e,f). The effective change of h_{Ni} by the magnetic field were estimated to be about 0.11 nm in samples 2 and 3, by fitting the vortex–antivortex movement to the theoretical calculation in Fig. 3b. In contrast, the trivial topological textures in samples 1 and 4 were barely affected by the external magnetic field (Supplementary Section 9). The consideration of imaginary component in the magneto-optic parameter of Ni offers precise analysis on the direction of the vortex–antivortex movement (Supplementary Section 10).

Magnetic-field-induced optical vortex–antivortex pair

Lastly, we demonstrated the magnetically induced generation and manipulation of the optical vortex–antivortex pair in the GTOC. We fabricated a GTOC of $h_{Ni} = 13$ nm (sample 5) that was close to the critical thickness ($h_{c2} = 13.15$ nm), where the transition between the non-trivial and trivial topological phases occurs. Sample 5 covered almost the same area in the generalized parameter space as sample 4 (Fig. 2b). Figure 4a,b shows the reflection amplitude and phase distribution of sample 5, depending on the external magnetic field (B) along the z axis. Upon applying a continuously varying global phase mathematically

(Supplementary Section 11), the phase distribution in Fig. 4b demonstrated the fork pattern at the location of the OVs. From $B = -0.5$ T to $B = 0$ T, the GTOC supported a single trivial reflection minimum and did not exhibit a fork-like pattern in the interferogram. As the external magnetic field changed from negative to positive, the optical thickness of the Ni layer decreased, and reached the critical thickness for the topological phase transition. At $B = 0.1$ T, the reflection amplitude was extremely suppressed, and a set of two fork patterns appeared in the holographic interferogram. The two fork patterns with opposite winding directions confirmed the presence of the optical vortex ($w = +1$) and antivortex ($w = -1$), respectively. As the magnetic field further increased from 0.1 T to 0.5 T, the fork patterns moved in opposite directions, and separate away.

Figure 4c schematically summarizes the experimental measurements of the magnetically induced generation and manipulation of the optical vortex–antivortex pair in the GTOC. The measured trajectory along which the optical vortex and antivortex moved matched the theoretical prediction at $h_{Ni} = h_{c2}$ (Fig. 3b). According to the parameter $\sigma\mathbf{w} \cdot \mathbf{M}$, the optical vortex and antivortex moved about 1.20 mm and about 1.17 mm, respectively, from the generation centre, in opposite directions, which correspond to the displacement (Δh_1, Δh_2) of (−2.23 nm, −0.72 nm) and (2.16 nm, 0.82 nm), respectively, in the generalized parameter space. Figure 4d shows the topological transition of the GTOC depending on the external magnetic field, from −0.5 T to 0.5 T. Owing to the paramagnetic behaviour of the Ni layer, the creation and annihilation of the optical vortex–antivortex pair in the current GTOC was reversible. It is worth noting that the employment of the ferromagnetic, out-of-plane magnetized layers[39,40] (platinum (Pt)/Co and Pt/Co/Pt) will provide the GTOC with the ability for hysteretic magneto-optically driven dynamics and topological information storage.

Discussion

In summary, we have experimentally demonstrated the spontaneous generation and magnetic-field-induced manipulation of an optical vortex–antivortex pair in a GTOC. The spontaneous generation and annihilation of the optical vortex and antivortex originated from the mathematical condition supporting the singular zero-reflection in the GTOC. Depending on the thickness of the Ni layer, the optical coupling of the top and bottom dielectric layers determined the presence or absence of the singularity. The magneto-optic effect on the Ni layer thus governed the abrupt, discontinuous transition between the trivial and non-trivial topological phases of the reflected light at the critical thickness. We also realized the magneto-optically driven dynamics of the vortex and antivortex singularities and their active control. We note that a lower external magnetic field or other different stimuli can also activate the dynamic characteristics of the GTOC platform by using ferromagnetism[39–41], electro- and thermo-optic effects[42,43], or electric gating[15,44,45] (Supplementary Section 12). We expect the further development of our methodology will be utilized to generate higher-order topological textures[46,47] (Supplementary Section 13), spatio-temporal electromagnetic singularities[48,49], and optical polarization and vortex knots[50–52].

Online content

Any methods, additional references, Nature Research reporting summaries, source data, extended data, supplementary information, acknowledgements, peer review information; details of author contributions and competing interests; and statements of data and code availability are available at https://doi.org/10.1038/s41586-022-05229-4.

1. Coullet, P., Gil, L. & Rocca, F. Optical vortices. *Opt. Commun.* **73**, 403–408 (1989).
2. Bliokh, K. Y., Rodríguez-Fortuño, F. J., Nori, F. & Zayats, A. V. Spin–orbit interactions of light. *Nat. Photon.* **9**, 796–808 (2015).
3. Grier, D. G. A revolution in optical manipulation. *Nature* **424**, 810–816 (2003).
4. Padgett, M. & Bowman, R. Tweezers with a twist. *Nat. Photon.* **5**, 343–348 (2011).
5. Schmiegelow, C. T. et al. Transfer of optical orbital angular momentum to a bound electron. *Nat. Commun.* **7**, 12998 (2016).
6. Bozinovic, N. et al. Terabit-scale orbital angular momentum mode division multiplexing in fibers. *Science* **340**, 1545–1548 (2013).
7. Nicolas, A. et al. A quantum memory for orbital angular momentum photonic qubits. *Nat. Photon.* **8**, 234–238 (2014).
8. Weber, M. et al. MINSTED fluorescence localization and nanoscopy. *Nat. Photon.* **15**, 361–366 (2021).
9. Beijersbergen, M. W. Helical-wavefront laser beams produced with a spiral phaseplate. *Opt. Commun.* **112**, 321–327 (1994).
10. Yu, N. et al. Light propagation with phase discontinuities: generalized laws of reflection and refraction. *Science* **334**, 333–337 (2011).
11. Chong, K. E. et al. Polarization-independent silicon metadevices for efficient optical wavefront control. *Nano Lett.* **15**, 5369–5374 (2015).
12. Deng, Z.-L. et al. Observation of localized magnetic plasmon skyrmions. *Nat. Commun.* **13**, 8 (2022).
13. Uhlíř, V. et al. Dynamic switching of the spin circulation in tapered magnetic nanodisks. *Nat. Nanotechnol.* **8**, 341–346 (2013).
14. Jenkins, A. S. et al. Spin-torque resonant expulsion of the vortex core for an efficient radiofrequency detection scheme. *Nat. Nanotechnol.* **11**, 360–364 (2016).
15. Kwon, W. J. et al. Sound emission and annihilations in a programmable quantum vortex collider. *Nature* **600**, 64–69 (2021).
16. Veshchunov, I. S. et al. Optical manipulation of single flux quanta. *Nat. Commun.* **7**, 12801 (2016).
17. Dobrovoloskiy, O. V. et al. Ultra-fast vortex motion in a direct-write Nb-C superconductor. *Nat. Commun.* **11**, 3291 (2020).
18. Mermin, N. D. The topological theory of defects in ordered media. *Rev. Mod. Phys.* **51**, 591 (1979).
19. Blatter, G. et al. Vortices in high-temperature superconductors. *Rev. Mod. Phys.* **66**, 1125 (1994).
20. Shinjo, T. et al. Magnetic vortex core observation in circular dots of permalloy. *Science* **289**, 930–932 (2000).
21. Chmiel, F. P. et al. Observation of magnetic vortex pairs at room temperature in a planar α-Fe_2O_3/Co heterostructure. *Nat. Mater.* **17**, 581–585 (2018).
22. Lagoudakis, K. G. et al. Quantized vortices in an exciton-polariton condensate. *Nat. Phys.* **4**, 706–710 (2008).
23. Ma, X. et al. Realization of all-optical vortex switching in exciton-polariton condensates. *Nat. Commun.* **11**, 897 (2020).
24. Indenbom, M. V. et al. Magneto-optical observation of twisted vortices in type-II superconductors. *Nature* **385**, 702–705 (1997).
25. Reimann, T. et al. Visualizing the morphology of vortex lattice domains in a bulk type-II superconductor. *Nat. Commun.* **6**, 8813 (2015).
26. Kosterlitz, J. M. & Thouless, D. J. Ordering, metastability and phase transitions in two-dimensional systems. *J. Phys. C* **6**, 1181 (1973).
27. Christodoulou, P. et al. Observation of first and second sound in a BKT superfluid. *Nature* **594**, 191–194 (2021).
28. Allen, L. et al. Orbital angular momentum of light and the transformation of Laguerre–Gaussian laser modes. *Phys. Rev. A* **45**, 8185 (1992).
29. Gorodetski, A. et al. Observation of the spin-based plasmonic effect in nanoscale structures. *Phys. Rev. Lett.* **101**, 043903 (2008).
30. Jin, J. et al. Topologically enabled ultrahigh-Q guided resonances robust to out-of-plane scattering. *Nature* **574**, 501–504 (2019).
31. Wang, B. et al. Generating optical vortex beams by momentum-space polarization vortices centred at bound states in the continuum. *Nat. Photon.* **14**, 623–628 (2020).
32. Situ, G. & Fleischer, J. W. Dynamics of the Berezinskii–Kosterlitz–Thouless transition in a photon fluid. *Nat. Photon.* **14**, 517–522 (2020).
33. Bruno, P., Dugaev, V. K. & Tailefumier, M. Topological Hall effect and Berry phase in magnetic nanostructures. *Phys. Rev. Lett.* **93**, 096806 (2004).
34. Jiang, W. et al. Direct observation of the skyrmion Hall effect. *Nat. Phys.* **13**, 162–169 (2017).
35. Heinze, S. et al. Spontaneous atomic-scale magnetic skyrmion lattice in two dimensions. *Nat. Phys.* **7**, 713–718 (2011).
36. Zheng, G. et al. Tailoring Dzyaloshinskii–Moriya interaction in a transition metal dichalcogenide by dual-intercalation. *Nat. Commun.* **12**, 3639 (2021).
37. Xu, S.-Y. et al. Topological phase transition and texture inversion in a tunable topological insulator. *Science* **332**, 560–564 (2011).
38. Sie, E. J. et al. An ultrafast symmetry switch in a Weyl semimetal. *Nature* **565**, 61–66 (2019).
39. Carcia, P. F. Perpendicular magnetic anisotropy in Pd/Co and Pt/Co thin-film layered structures. *J. Appl. Phys.* **63**, 5066 (1988).
40. Kim, D. et al. Extreme anti-reflection enhanced magneto-optic Kerr effect microscopy. *Nat. Commun.* **11**, 5937 (2020).
41. Huang, B. et al. Layer-dependent ferromagnetism in a van der Waals crystal down to the monolayer limit. *Nature* **546**, 270–273 (2017).
42. Hu, Y. et al. On-chip electro-optic frequency shifters and beam splitters. *Nature* **599**, 587–593 (2021).
43. Kita, D. M. et al. High-performance and scalable on-chip digital Fourier transform spectroscopy. *Nat. Commun.* **9**, 4405 (2018).
44. Lopez-Sanchez, O. et al. Ultrasensitive photodetectors based on monolayer MoS_2. *Nat. Nanotechnol.* **8**, 497–501 (2013).
45. Yu, Y. et al. Giant gating tunability of optical refractive index in transition metal dichalcogenide monolayers. *Nano Lett.* **17**, 3613–3618 (2017).
46. Sroor, H. et al. High-purity orbital angular momentum states from a visible metasurface laser. *Nat. Photon.* **14**, 498–503 (2020).

47. Bahari, B. et al. Photonic quantum Hall effect and multiplexed light sources of large orbital angular momenta. *Nat. Phys.* **17**, 700–703 (2021).
48. Zdagkas, A. et al. Observation of toroidal pulses of light. *Nat. Photon.* **16**, 523–528 (2022).
49. Shen, Y., Hou, Y., Papasimakis, N. & Zheludev, N. I. Supertoroidal light pulses as electromagnetic skyrmions propagating in free space. *Nat. Commun.* **12**, 5891 (2021).
50. Larocque, H. et al. Reconstructing the topology of optical polarization knots. *Nat. Phys.* **14**, 1079–1082 (2018).
51. Dennis, M. R. et al. Isolated optical vortex knots. *Nat. Phys.* **6**, 118–121 (2010).
52. Wang, K., Dutt, A., Wojcik, C. C. & Fan, S. Topological complex-energy braiding of non-Hermitian bands. *Nature* **598**, 59–64 (2021).

Methods

Sample fabrication

A 100-nm-thick Al mirror was prepared on a 2 cm × 2 cm Si substrate by thermal evaporation. The height-varying SiO_2 layers were achieved by radio-frequency sputtering, taking advantage of the directionality of the deposition process. Therefore, the SiO_2 layers exhibited a gradual change in thickness over the sample, with the direction and range of the thickness gradient depending on the orientation and position of the sample with respect to the centre of the deposition pattern. Further information on the thickness distribution and gradient in the SiO_2 can be found in Supplementary Section 4. To maximize the SiO_2 thickness range over the sample, the substrate was placed 3 cm away from the centre of the sample holder. The sample was rotated by 90° between the depositions of the top and bottom SiO_2 layers, so that the thickness gradients of the two layers were almost perpendicular. A magnetic Ni layer with uniform thickness was deposited uniformly over the sample area using electron-beam evaporation.

Measurement set-up

The confocal microscope scanned an area of 9 mm × 9 mm, by using a motorized *XYZ* stage. We used reflective optical elements, including a right-angle metal prism mirror for beam splitting, and a concave metal mirror for beam focusing, to minimize undesired scattering and back-reflection, and to improve the measurement precision. The optical readout system employing an femtowatt photoreceiver (Newport 2151) and a high-precision data acquisition tool (NI-DAQ PCIe-6321) provided a sufficiently high dynamic range to measure the reflection singularities. The off-axis holography set-up was based on an interferometric imaging system. The propagation direction of the reference beam with a 1° tilt interfered with the signal beam reflected from the GTOC. The numerical post-process filtering in the Fourier space retrieved the complex reflection coefficient distribution from the acquired interference pattern (Supplementary Section 5). The magneto-optic effects on the Ni layer were induced using a permanent neodymium magnet. A motorized translation stage moved the magnet, and controlled the applied magnetic field to the sample. We measured the complex refractive index and the Voigt parameter, respectively, employing the conventional spectroscopic ellipsometry and the home-built cross-polarized reflectance measurement set-up combined with an external magnet (Supplementary Section 2).

Data availability

The data that support the findings of this study are available from the corresponding authors upon reasonable request.

Code availability

All codes generated during this study are available upon request from the corresponding authors.

Acknowledgements We thank S. Lee, D. Kim, S. Park and H. Oh for discussions. M.-K.S. acknowledges the support of the KAIST Cross-Generation Collaborative Lab project and the National Research Foundation of Korea (NRF) (2020R1A2C2014685 and 2020R1A4A2002828). J.S. acknowledges the support of the NRF (2021R1A2C200868711). D.K. acknowledges the support of the NRF (2015H1A2A1033753 and 2019R1A6A1A10073887). Y.-S.C. acknowledges the support of the NRF (2020R1I1A1A01069219).

Author contributions D.K. conceived the idea. A.B. and D.K. designed and fabricated the gradient-thickness optical cavity samples. D.K. and Y.-S.C. built the magneto-optic off-axis holography set-up. D.K. performed the magneto-optic measurements and the theoretical calculations. D.K. and M.-K.S. analysed the data and wrote the manuscript with input from all other authors.

Competing interests The authors declare no competing interests.

Additional information
Supplementary information The online version contains supplementary material available at https://doi.org/10.1038/s41586-022-05229-4.
Correspondence and requests for materials should be addressed to Dongha Kim or Min-Kyo Seo.
Peer review information *Nature* thanks Haoran Ren, Lei Shi and the other, anonymous, reviewer(s) for their contribution to the peer review of this work. Peer reviewer reports are available.

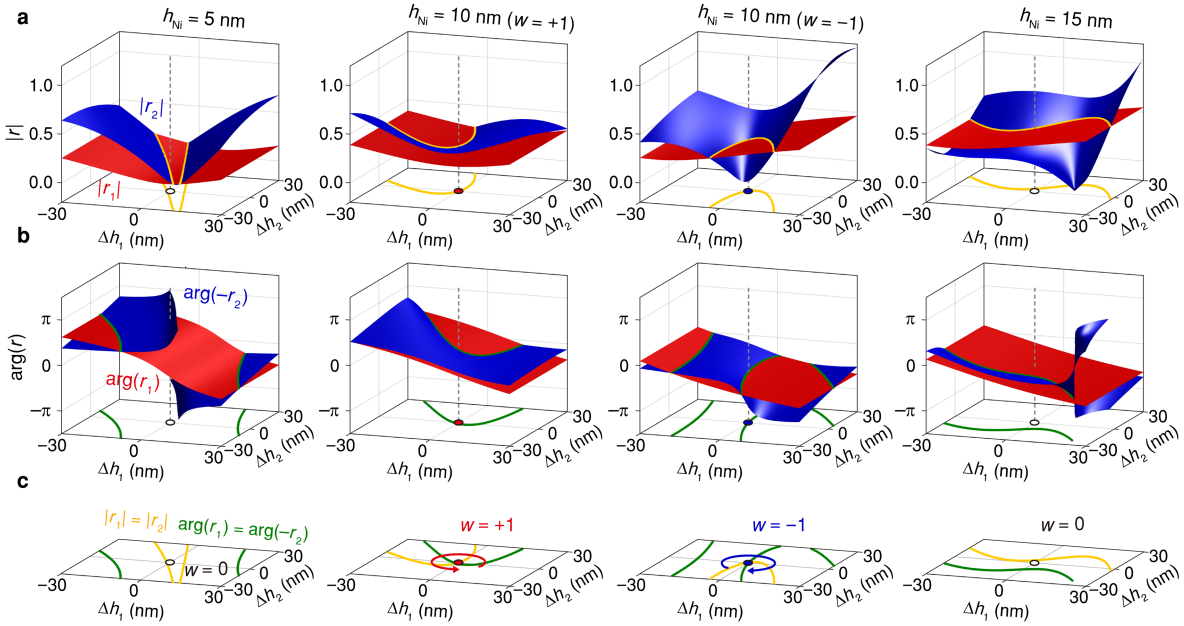

Extended Data Fig. 1 | Amplitude and phase distribution of the calculated reflection coefficient components (r_1 and r_2) in the generalized parameter space (h_1, h_2). a,**b**, Plot of the (**a**) amplitude and (**b**) phase of the reflection coefficient components r_1 (the red curved surface) and r_2 (the blue curved surface) near the reflection minima in the generalized parameter space for the GTOCs with h_{Ni} = 5, 10, and 15 nm. (Δh_1, Δh_2) represents the position away from the target reflection minimum in the generalized parameter space. The yellow and green solid curves represent the same amplitude ($|r_1| = |r_2|$) and out-of-phase conditions ($\arg(r_1) = \arg(-r_2)$), respectively. **c**, Projection of the same amplitude (the yellow curve) and out-of-phase (the green curve) conditions onto the generalized parameter space. The singular minimum of reflection for the non-trivial topological textures exists only when the two conditions intersect. The red and blue dots indicate the intersections for the optical vortex (w = +1) and antivortex (w = −1), respectively. The white circles indicate the positions of the weak reflection minima of the trivial topological phase (w = 0).

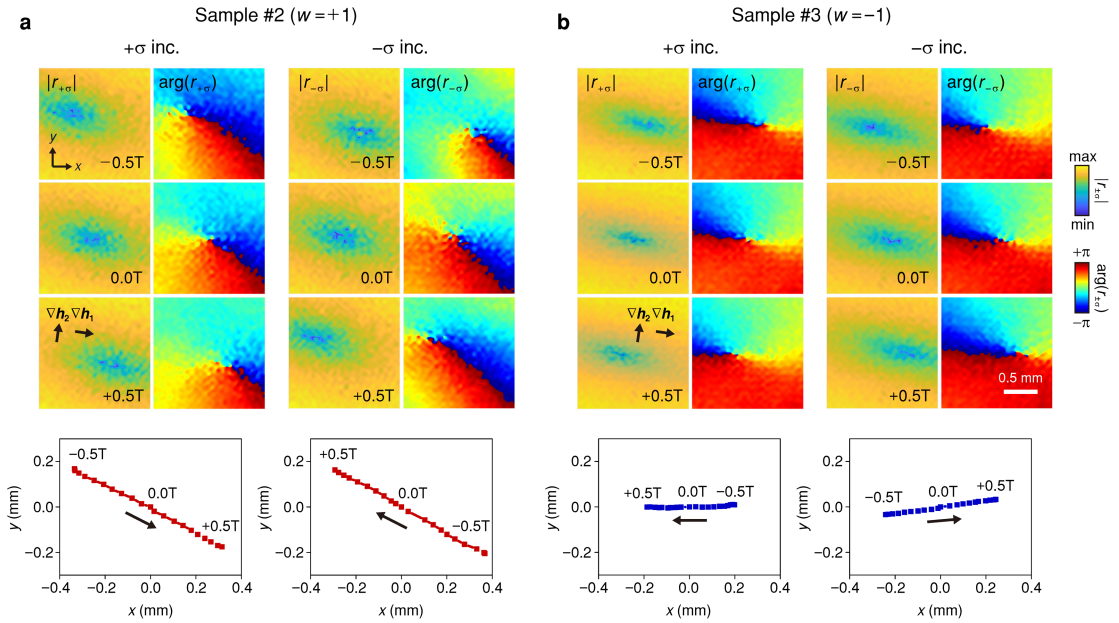

Extended Data Fig. 2 | Polarization dependency of magneto-optically-driven optical vortex dynamics. a,**b**, External magnetic-field-dependent behaviour of the complex reflection coefficient of the (**a**) optical vortex (Sample #2, $w = +1$) and (**b**) antivortex (Sample #3, $w = -1$) for the opposite handedness of the circular polarization (+σ and −σ) of the incident light.